Ashani *et al. Energy Mater.* **2025**, *5*, 500111
DOI: 10.20517/energymater.2025.10

Energy Materials

Article

Open Access

Check for updates

Giant spin Seebeck effect in two-dimensional V_2S_2O altermagnet

Timothy M. Ashani[#], Abdullah[#], Jisang Hong[*]

Department of Physics, Pukyong National University, Busan 48513, Korea.
[#]Authors contributed equally.

[*]**Correspondence to:** Prof. Jisang Hong, Department of Physics, Pukyong National University, Busan 48513, Korea. E-mail: hongj@pknu.ac.kr

How to cite this article: Ashani, T. M.; Abdullah; Hong, J. Giant spin Seebeck effect in two-dimensional V_2S_2O altermagnet. *Energy Mater.* **2025**, *5*, 500111. https://dx.doi.org/10.20517/energymater.2025.10

Received: 6 Feb 2025 **First Decision:** 11 Mar 2025 **Revised:** 1 Apr 2025 **Accepted:** 17 Apr 2025 **Published:** 21 May 2025

Academic Editor: Sen Xin **Copy Editor:** Ping Zhang **Production Editor:** Ping Zhang

Abstract

Altermagnet is an uncommon category of antiferromagnets distinguished by their non-overlapping spin-bands, drawing significant attention from researchers. However, while reports on their electronic and magnetic properties are increasing rapidly, the study on the transport properties is still in early stage. Therefore, we explored the orientational spin-dependent transport features of altermagnet V_2S_2O using Boltzmann transport technique. This altermagnet had 1.15 eV direct band gap energy and a critical temperature of 746 K. We obtained a directional spin-dependent feature in the band structure whose effect spans through all the spin-dependent transport parameters. We found a low isotropic lattice thermal conductivity of magnitude 0.2 $Wm^{-1}K^{-1}$ at 300 K. Above all, the V_2S_2O altermagnet displayed a giant spin-dependent Seebeck coefficient of about 1.8 mVK^{-1} at 300 K and at a small electron or hole doping. This value is multiple times greater than reported values for most transport materials. Besides, we also found a maximum figure of merit of 0.86 in the hole-doped systems. Thus, our findings suggest the possibility of pure spin current generation for possible applications in spintronics and thermoelectricity.

Keywords: Spintronic, spin-dependent, altermagnetic material, spin-polarized band, and transport properties

INTRODUCTION

Altermagnetic (AM) materials are symmetry-compensated antiferromagnets whose band structures are characterized by spin splitting[1]. This implies that over the entire Brillouin zone, the up and down spin

bands of the AM materials do not entirely overlap. Rather, the band structure exhibits orientational-dependent splitting. The spin-orbit coupling (SOC)-induced magnetic property has been the cornerstone of spintronic applications such as spin-orbit torque, spin transistors, topological insulators, and the spin Hall effect[2,3]. Nevertheless, the swift decoherence of spin-polarized electrons caused by SOC restricts the broad applications of these materials[4]. In contrast, spin splitting has been achieved in AM materials without applying SOC[5-7]. The source of the spin splitting in AM materials is the magnetic space group, which is protected by crystal symmetry[8,9]. This spin-splitting allows the realization of highly spin-polarized currents[8,10]. The study of AM materials is still in its infancy; however, it may be a fertile field for theory and potential applications. For example, the unique band feature in AM materials may make them potential materials for thermal transport devices, valleytronics, field-effect electronics, photo-magnetism, spin caloritronics, spin transfer torque, superconductivity, and spintronic applications[9-12]. The AM materials also have the potential for high-speed device operation because of their ultra-high dynamic speed and zero net magnetic moment, allowing resistance to external magnetic disturbance[13]. Several bulk materials, such as RuO_2, $FeSb_2$, FeF_2, MnTe, Ve_2Te_2O, MnF_2, MnO, CoF_3, MnO_2, $NaFeO_2$, NdB_2C_2, and some $GdFeO_3$-type perovskites, have been predicted to be AM materials[13-16].

In parallel with the discovery of the AM behavior in RuO_2 and other bulk materials, it has been predicted that two-dimensional (2D) materials such as Mn_2ClI, V_2S_2O, $MnTeMoO_6$, V_2F_7Cl, Cr_2SO, V_2SeTeO, Cr_2O_2, $CrMoC_2S_6$, Mn_2ClF, RuF_4, and Cr_2SeO can also display an AM behavior[4-6,17,18]. However, most studies have concentrated on basic unconventional properties with minimal reports on thermoelectricity in AM materials[19-24]. Recently, Sukhachov *et al.* suggested that AM materials could be employed for effective thermoelectricity[25]. Using the AM spin-splitting effect, Bai *et al.* also reported efficient spin-charge conversion in RuO_2 altermagnet[26]. Besides, Lyu and Li pointed out that the transport properties in AM materials were directional dependent[27]. Indeed, the AM behavior has been experimentally confirmed in RuO_2 and MnTe using angle-resolved photoemission spectroscopy[28,29]. Fan *et al.* also reported experimental work that the AM spin splitting effect could produce anisotropic spin currents in AM material with polarization, which depends on the crystal orientation of the material[30]. Moreover. Bai *et al.* also reported a few microvolts in altermagnet RuO_2 spin-charge conversion efficiency using spin Seebeck effect measurement[26]. Motivated by the predicted potentials of unconventional spin-splitting effect in AM materials, we propose to leverage directional spin-dependent thermoelectric properties and predict a massive spin-Seebeck coefficient in V_2S_2O monolayer AM material.

Indeed, thermoelectricity is a fertile field for testing and predicting high-performance transport materials via theory-based material search techniques. Although precise prediction of these high-performance transport materials computationally entails vigorous optimization, the experimental approach is even more complicated. In our work, we inspect the orientational spin-dependent transport properties at finite temperatures and aim to propose a giant spin Seebeck effect in the V_2S_2O altermagnet for the spin-polarized current generation in spintronics and thermoelectric device applications.

THEORETICAL METHODS

All our calculations were conducted in this work using the spin-polarized density functional theory as implemented in the Vienna ab initio simulation package (VASP)[31,32]. We used the Perdew, Burke, and Ernzerhof parametrization within the generalized gradient approximation for an exchange functional[33], including the van der Waals interaction[34] as a correlation functional. A plane wave basis set is employed with an energy cutoff of 600 eV. The energy and force convergence criteria are set to 10^{-6} eV and 10^{-3} eV/Å, respectively. A well-converged Monkhorst-Pack scheme-generated k-point mesh of 10 × 10 × 1, which also ensures the convergence of the energy and force, was used[35]. Furthermore, we applied a vacuum distance of

25 Å along the z-axis to prevent adjacent units' interaction. The Heyd-Scuseria-Ernzerhof screened hybrid functional was used to calculate the spin-polarized electronic band structure[36,37]. To estimate the critical temperature, we applied a simulation of the field cooling and Landau-Lifshitz-Gilbert Huen method as implemented in the VAMPIRE simulation package[38] for the temperature-dependent sub-lattice magnetization calculation. To this end, a supercell of 100 × 100 × 1 with total time steps of 100,000 and 0.1 fs is used. Our directional spin-dependent transport properties were explored using the BoltzTraP code[39]. Since most of the transport properties are carrier relaxation time (τ) dependent, we considered the scattering contributions from the impurity effects (τ_{imp}) polar optical phonon (τ_{opt}), and acoustic phonon (τ_{aco}). Therefore, the total τ, which depends on energy and temperature, can be expressed as:

$$\tau(T,E)^{-1} = \tau_{imp}^{-1} + \tau_{opt}^{-1} + \tau_{aco}^{-1} \quad (1)$$

In addition, we also computed the lattice part of the thermal conductivity with phono3py code[40] using a 4 × 4 × 1 supercell, 6 × 6 × 1 K-mesh, and energy cutoff 600 eV.

RESULTS AND DISCUSSION

Figure 1A reveals the side and top views of monolayer V_2S_2O. The red and black colors denote vanadium atoms with spin-up and spin-down, while the blue and yellow colors represent the oxygen and sulfur atoms. The monolayer V_2S_2O has a tetragonal crystal structure and a space group of P4mmm (123). We obtained the lattice constants of a = b = 3.84 Å after structure optimization. The monolayer V_2S_2O is made of a V_2O plane embedded by two S planes with interatomic distances of 1.921 Å and 2.479 Å from V to O and S. This shows that the V_2S_2O monolayer exhibits high-degree symmetry along in-plane and out of plane. Note that the thermal stability, cleavage energy, and dynamic stability were already reported elsewhere[41]. To investigate the magnetic ground state of monolayer V_2S_2O, we considered ferromagnetic (FM) and three different antiferromagnetic (AFM) spin configurations in a supercell of dimension 2 × 2 × 1. In Figure 1B-D, we show the different AFM spin configurations. The most stable AFM-Neel state was obtained [Figure 1B], and the energy difference (E_{ex}) between this state and the FM state ($E_{ex} = E_{FM} - E_{AFM}$) was 536 meV/unit cell. Each V atom had an atomic magnetic moment of magnitude 1.7 μ_B. However, the net magnetic moment of the unit cell vanishes due to the anti-parallel coupling between the V atoms. The AFM-Neel ground state in the V_2S_2O monolayer is consistent with other theoretical reports[6,41]. Figure 1E reveals the electronic band structure without SOC. This electronic band structure shows a spin splitting around the X and Y points, while in other parts of the Brillouin zone, both spin-down (↓) and spin-up (↑) bands were completely overlapped. The spin splitting at X and Y points was 0.51 eV at the valence band maximum. AM V_2S_2O monolayer also showed a semiconducting behavior with a direct band gap of 1.15 eV at the Y and X points. We also computed the critical (Neel) temperature via the model of Heisenberg spin Hamiltonian[42] based on:

$$H_{ex} = -\sum_{i \neq j} J_{ij}(S_i \cdot S_j) - k_u(S_i \cdot e)^2 \quad (2)$$

$$n_\alpha = \frac{1}{N_\alpha}\sum_i^{N_\alpha} S_i \quad (3)$$

Here, S_i and S_j are the spin moment direction of atoms at the neighboring sites i and j, J_{ij} is the exchange interaction between atoms at the neighboring sites, and k_u is the anisotropy energy per atom. Meanwhile, N_α and n_α represent the number of atoms in the sublattice and the mean of sublattice magnetization of each atom. Using E_{ex}, the difference between the total energies of the FM and AFM spin states, we extracted the exchange interaction via the relation:

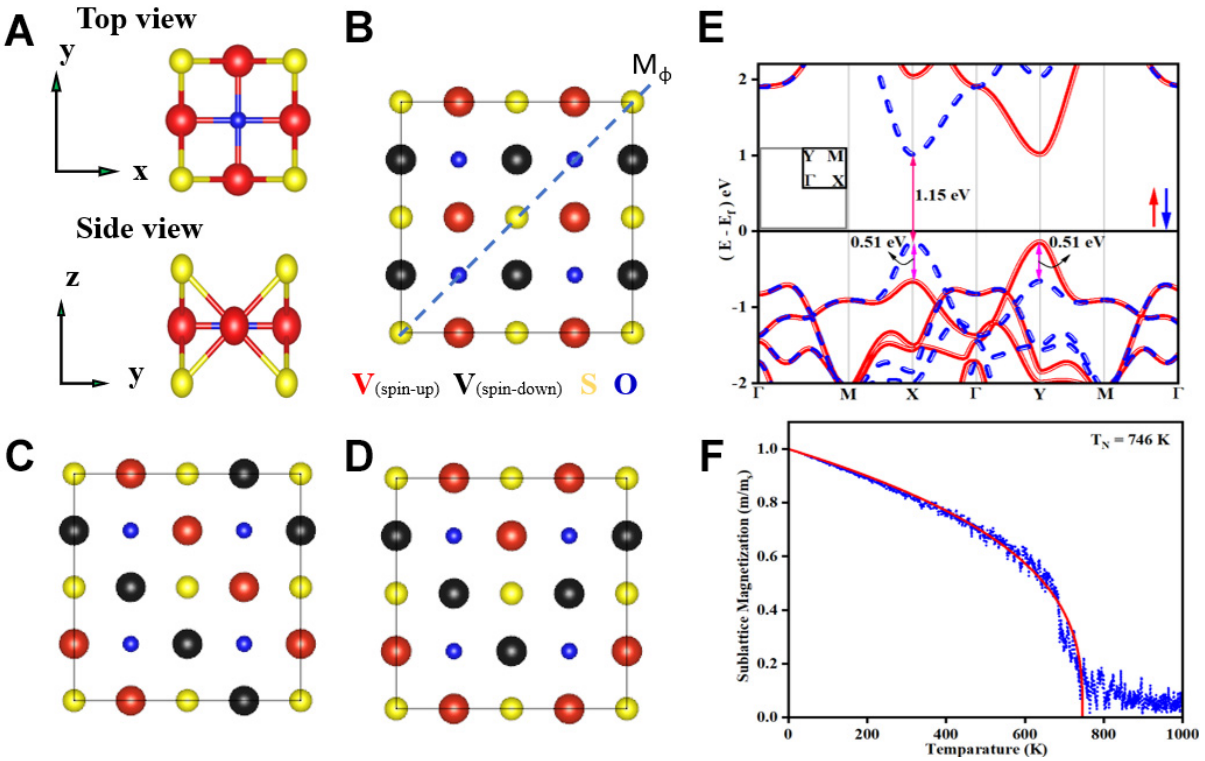

Figure 1. (A) Schematic illustration of top and side views of V_2S_2O monolayer. Magnetic configurations of (B) AFM-Neel, (C) AFM-Stripy, and (D) AFM-Zigzag in a 2 × 2 × 1 supercell; (E) Band structure of monolayer V_2S_2O with First Brillouin zone with high symmetry points as inset (red lines for spin-up and blue dashed-lines for spin-down); (F) Temperature-dependent sublattice magnetization of V_2S_2O monolayer. AFM: Antiferromagnetic.

$$J_{ij} = \frac{E_{ex}}{Nm^2} \tag{4}$$

where m and N are the average magnetic moment and the number of magnetic atoms in the system. Figure 1F shows the temperature-dependent sublattice magnetization curve. Overall, we obtained a Neel temperature of 746 K for the V_2S_2O monolayer.

Now, we explore the spin-dependent transport properties such as spin-dependent Seebeck coefficients, electrical conductivity, electronic thermal conductivity (K_e), and lattice thermal conductivity (K_L). First, the spin-dependent Seebeck coefficient [$S^{(\uparrow\downarrow)}$] is obtained using:

$$S^{(\uparrow\downarrow)} = \frac{1}{qT}\frac{L_1^{(\uparrow\downarrow)}}{L_0^{(\uparrow\downarrow)}} \tag{5}$$

Here, q, T, and L are the elementary charge, the temperature, and the generalized linear spin-dependent transport coefficient expressed as:

$$L_n^{(\uparrow\downarrow)}(\mu;T) = q^2 \int \sigma^{(\uparrow\downarrow)}(i,k)(\varepsilon - \mu)^n \left(-\frac{\partial f(\varepsilon;\mu,T)}{\partial \varepsilon}\right) d\varepsilon \tag{6}$$

The conductivity tensor over the bands (i) and the k-points (k) can be expressed as $\sigma^{(\uparrow\downarrow)}(i,k) = e^2\tau i,kV^2$, where V represents group velocity. Figure 2 reveals the spin-dependent Seebeck coefficients for the spin-up channel ($S^{\uparrow}$) and spin-down channel ($S^{\downarrow}$). In the x-direction, the Seebeck coefficient of the spin-down channel comes first before the spin-up channel Seebeck coefficient in both doped systems. Meanwhile, in

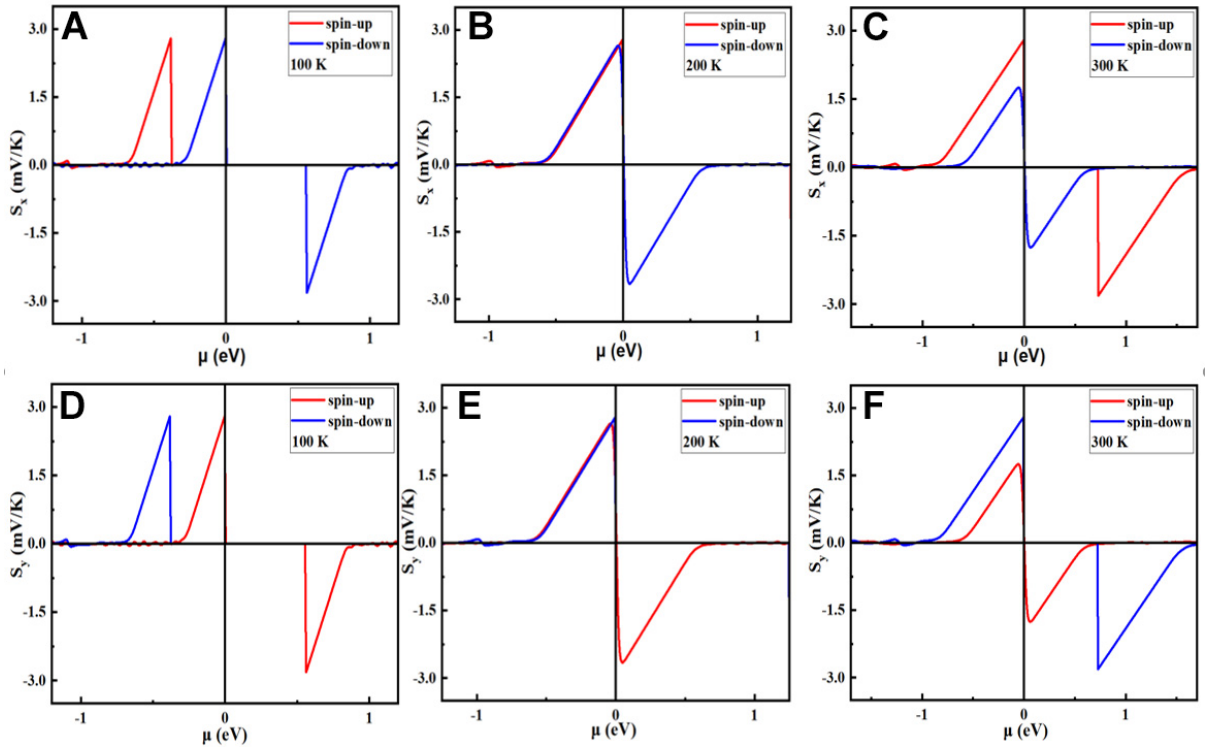

Figure 2. Spin-dependent Seebeck coefficient ($S^{\uparrow}$ and $S^{\downarrow}$) along x-direction at (A) 100 K *vs.* chemical potentials; (B) 200 K *vs.* chemical potentials; (C) 300 K *vs.* chemical potentials; and y-direction at (D) 100 K *vs.* chemical potentials; (E) 200 K *vs.* chemical potentials; and (F) 300 K *vs.* chemical potentials.

the y-direction, the Seebeck coefficient of the spin-up channel appears first before the spin-down component in both the electron and hole-doped systems. This feature is the direct consequence of the directional spin-dependent band structure in Figure 1E.

Note that the spin Seebeck coefficient does not depend on τ. However, other transport properties, such as electronic thermal and electrical conductivities, strongly depend on it. Hence, it is crucial to estimate τ accurately. Nonetheless, in most studies, the energy-independent constant relaxation time approach has been adopted with limitations in accounting for some scattering effects. This usually results in an overestimation of the thermoelectric performance. To remedy this, in our study, we applied the temperature-energy dependent relaxation time considering the contributions from the acoustic and optical phonons as implemented in the works of Casu *et al.* and Marfoua *et al.*[43,44]. Besides, we also considered the impurity scattering effect using the relation of Brooks-Herring. Note that the impurity scattering effect can be written as:

$$P_{imp}(T,E) = \frac{\pi n_I Z_I^2 e^4 E^{-3/2}}{\sqrt{2m}\,(4\pi\epsilon_o\epsilon_s)^2}\left[log\left(1+\frac{1}{x}\right)-\frac{1}{1+x}\right] \quad (7)$$

where the Z_I, n_I, ϵ_s, ϵ_o and m represent the impurity charge, the ionized impurity concentration, the relative dielectric constant, the vacuum's permittivity, and the effective mass, respectively. Also, $x = \frac{\hbar^2 q_0^2}{8mE}$ where q_o denotes Debye screening wave vector. The optical polar scattering can be estimated by:

$$P_{opt}(T,E) = \sum_i \frac{C\left(T,E,e_i^{LO}\right)-A\left(T,E,e_i^{LO}\right)-B\left(T,E,e_i^{LO}\right)}{Z\left(T,E,e_i^{LO}\right)E^{3/2}} \quad (8)$$

where the sum is over all longitudinal optical polar phonons with energy e_i^{LO} according to the Ridley model[39]. The contribution from the acoustic phonon scattering is obtained from:

$$P_{aco}(T,E) = \frac{(2m)^{3/2}k_BTD^2\sqrt{E}}{2\pi\hbar^4\rho v^2} \quad (9)$$

where D, ρ, v, E, and m are the band energy deformation potential, mass density, the sound average velocity, the energy of the electron, and the effective mass, respectively. To estimate the energy and temperature dependent τ, the intrinsic material quantities such as the dominant longitudinal optical phonon frequency ($\hbar\omega_{LO}$), high-frequency dielectric and lattice dielectric constants (ε_∞ and ε_L), deformation potential (DP), mass density (ρ), the average velocity of sound (v), and the effective mass ratio (m^*/m) of the system are required. We present all these parameters in Tables 1 and 2 for the spin-up and spin-down channels, respectively.

We present the temperature and spin-dependent carrier relaxation time along the y-direction (τ_y) and x-direction (τ_x) in Supplementary Figures 1A-F and 2A-D shows the contributions to the carrier relaxation time from different scattering effects. We found that the spin-down (spin-up) carrier had a longer τ along the x-direction (y-direction) in both electron and hole-doped systems. This can be attributed to the effect of the effective mass. As displayed in Tables 1 and 2, the spin-up (spin-down) carrier possessed relatively lower effective mass along the y-direction (x-direction). We further analyzed the scattering mechanisms due to impurity, optical polar, and acoustic phonon scatterings. As revealed in Supplementary Figure 2A-D, the τ was mainly affected by optical polar scattering. We now discuss the spin and temperature-dependent electrical conductivity [$\sigma^{(\uparrow\downarrow)}$]. Here, $\sigma^{\downarrow}$ and $\sigma^{\uparrow}$ are the electrical conductivities of carriers of the up and down spin channels. The spin-dependent electrical conductivity is computed using:

$$\sigma^{(\uparrow\downarrow)} = L_0^{(\uparrow\downarrow)} \quad (10)$$

Figure 3A and B reveals the temperature and spin-dependent electrical conductivity as a function of chemical potential. In the x-direction, the electrical conductivity was entirely influenced by the carriers of spin-down (blue color) because the contribution from the spin-up channel carriers (red color) was negligible. Meanwhile, in the y-direction, the opposite behavior was found. This behavior originates from the electronic band structure where the spin-down (spin-up) channel controls the bandgap in the x direction (y-direction). Besides, we found that the hole-doped system showed higher electrical conductivity than the electron-doped structure. For instance, in the x-direction and in room temperature, the σ of the spin-down carriers was 3.93×10^4 $(\Omega\ m)^{-1}$ and 1.5×10^4 $(\Omega\ m)^{-1}$ for the hole and electron-doped systems at a chemical potential of ±0.49. Similarly, in the y-direction these values became 3.22×10^4 and 1.23×10^4 $(\Omega\ m)^{-1}$, respectively, for the spin-up carriers at the same conditions. We attribute this carrier type dependency to the effect of the effective mass as displayed in Tables 1 and 2.

$$S_{eff-spin} = \frac{\sigma^{\uparrow}S^{\uparrow}-\sigma^{\downarrow}S^{\downarrow}}{\sigma^{\uparrow}+\sigma^{\downarrow}} \quad (11)$$

$$S_{eff-charge} = \frac{\sigma^{\uparrow}S^{\uparrow}+\sigma^{\downarrow}S^{\downarrow}}{\sigma^{\uparrow}+\sigma^{\downarrow}} \quad (12)$$

Next, we calculate the total effective spin-dependent Seebeck coefficient ($S_{eff\text{-}spin}$) and effective charge-dependent Seebeck coefficient ($S_{eff\text{-}charge}$) by associating the spin-dependent Seebeck coefficients with spin-dependent σ. These Seebeck coefficients are expressed as:

Table 1. The calculated intrinsic parameters for hole and electron carriers in the spin-up channel for the energy and temperature-dependent relaxation time

Orientation	Carrier type	DP	m*/m	V (ms^{-1})	ε_∞	ε_L	P (kgm^{-3})	$\hbar\omega_{LO}$ (meV)
x	Hole	2.59	0.14	7752	1.89	3.67	3410	70
	Electron	1.09	0.13	7752	1.89	3.67	3410	70
y	Hole	3.05	0.09	7752	1.89	3.67	3410	70
	Electron	1.69	0.12	7752	1.89	3.67	3410	70

DP: Deformation potential.

Table 2. The calculated intrinsic parameters for the energy-dependent relaxation time in the spin-down channel for hole and electron carriers

Orientation	Carrier type	DP	m*/m	V (ms^{-1})	ε_∞	ε_L	P (kgm^{-3})	$\hbar\omega_{LO}$ (meV)
x	Hole	3	0.09	7752	1.89	3.67	3410	70
	Electron	1.64	0.11	7752	1.89	3.67	3410	70
y	Hole	2.64	0.15	7752	1.89	3.67	3410	70
	Electron	1.14	0.16	7752	1.89	3.67	3410	70

DP: Deformation potential.

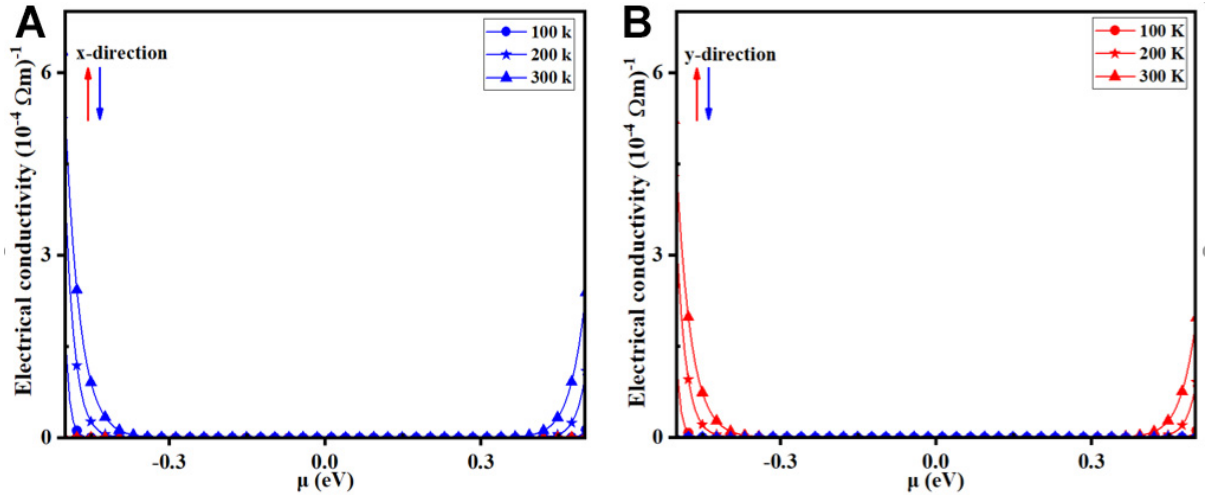

Figure 3. Spin-dependent electrical conductivities along (A) x-direction and (B) y-direction at different temperatures.

Figure 4A-D reveals the computed results. Along the x-direction (y-direction), the $S_{eff\text{-}spin}$ and $S_{eff\text{-}charge}$ are determined by the spin-down carriers (spin-up carrier) since $\sigma^{\uparrow}(\sigma^{\downarrow})$ is negligible. Due to this feature, we expect the generation of a pure spin-polarized current in a particular direction when a heat gradient is applied along that direction. At 300 K, we obtained a maximum $S_{eff\text{-}spin}$ of 1.8 mV/K in both electron and hole-doped systems along the x and y directions. Note that both $S_{eff\text{-}spin}$ and $S_{eff\text{-}charge}$ have approximately the same magnitude at all temperatures along the x and y directions. This feature results from the negligible value of either $\sigma^{\uparrow}$ or $\sigma^{\downarrow}$ along each direction as discussed earlier. Indeed, we achieved a giant effective Seebeck coefficient in the V_2S_2O monolayer altermagnet compared with previously reported structures. For instance, the maximum spin Seebeck coefficients reported for GaMnAs, Pt/YIG, Cr_2O_3, HfMnGe, $EuTiO_3$ and V_2SeTeO monolayers are ~5 μV/K, ~6 μV/K, 20 μV/K, ~80 μV/K, 0.1 mV/K, and 0.64 mV/K respectively at room temperature[45-49].

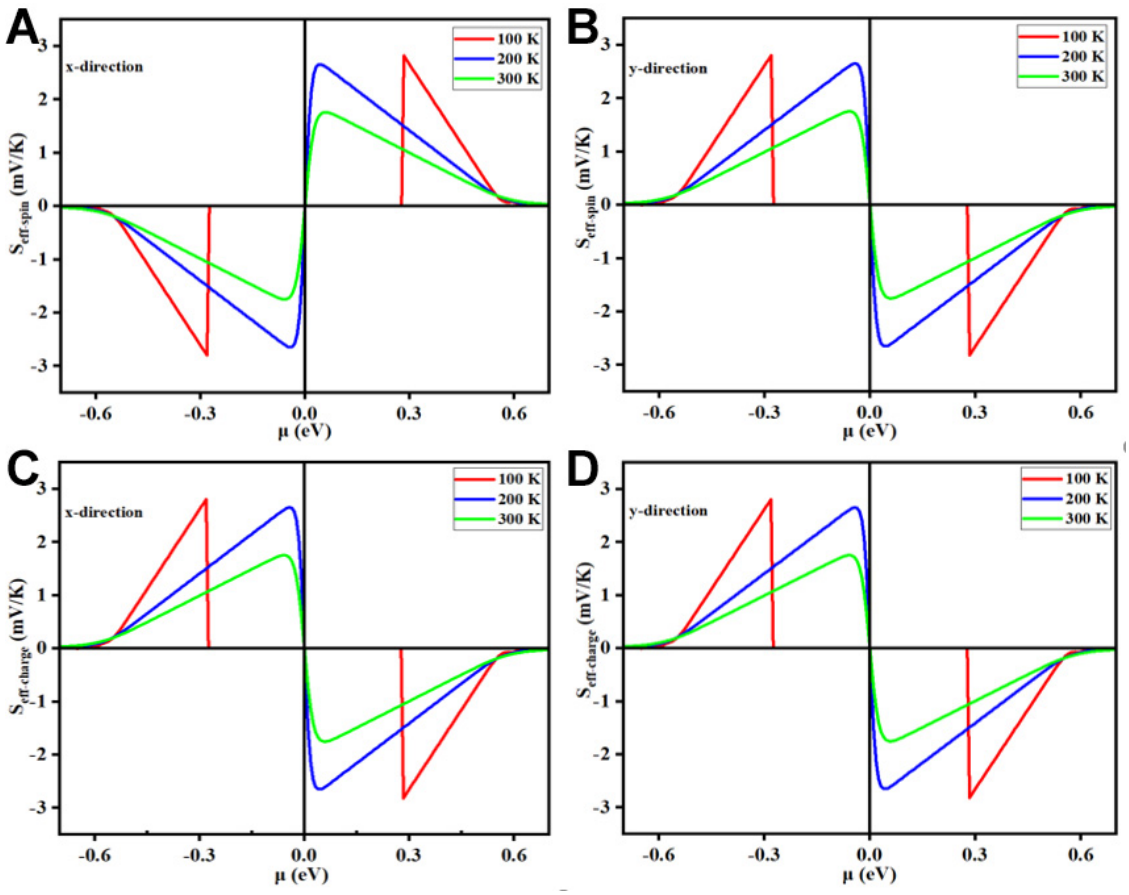

Figure 4. Effective spin Seebeck coefficients at different temperatures in (A) x-direction *vs.* chemical potentials and in (B) y-direction *vs.* chemical potentials, and effective charge Seebeck coefficients in (C) x-direction *vs.* chemical potentials, and in (D) y-direction *vs.* chemical potentials.

We also investigated the electronic and lattice thermal conductivities. Figure 5A and B shows the K_e for the spin-up (red color) and spin-down (blue color) carriers along the x-direction and y-direction as a function of temperature and chemical potential. Similar to the σ, the electronic part of the thermal conductivity is also entirely determined by either of the spin carriers depending on the direction under consideration. To be precise, the spin-up (spin-down) carriers were wholly responsible for the Ke in the y-direction (x-direction). Also, the K_e in the hole-doped system was greater than that of the electron-doped system. This may also be linked to the relaxation time disparity between the two regions. The spin-down carriers had K_e of 2.24 $Wm^{-1}K^{-1}$ in the hole-doped system, while it became 0.49 $Wm^{-1}K^{-1}$ in the electron-doped system at 300 K with chemical potentials of ±0.49. Meantime, the spin-up channel carriers had Ke of 1.83 $W.m^{-1}K^{-1}$ in the hole-doped system and 0.41 $Wm^{-1}K^{-1}$ in the electron-doped system at the same conditions.

The K_L is given by:

$$K_L = \frac{1}{NV} \sum_i C_i v_i^2 \tau_i \quad (13)$$

where τ_i, v_i, and C_i are the phonon lifetime, group velocity, and mode heat capacity. Besides, the phonon mode, number of unit cells, and volume of the system are represented with i, N, and V. Figure 5C shows the lattice part of the thermal conductivity of the V_2S_2O monolayer along the x and y directions. The K_L was

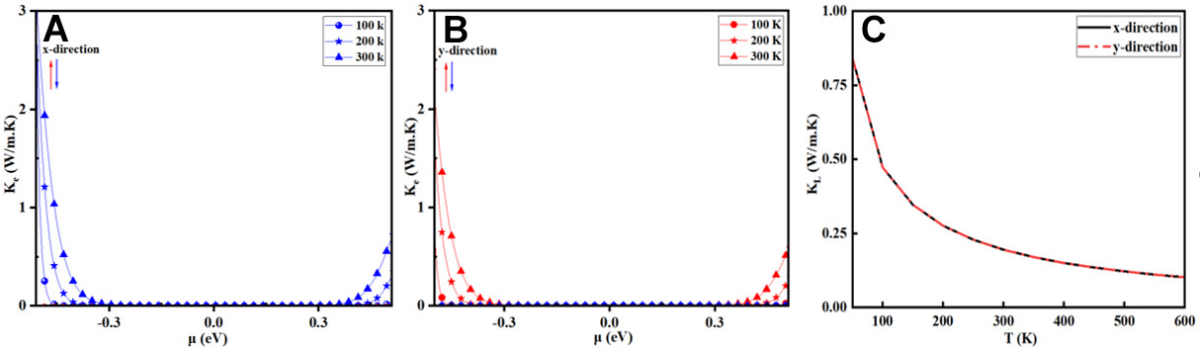

Figure 5. Electronic thermal conductivity along (A) x-direction and (B) y-direction for spin-up and spin-down at different temperatures (red color for spin-up and blue color for spin-down); (C) The lattice thermal conductivity *vs.* temperature along x-direction (color black) and y-direction (color red).

decreased with increasing temperature. This behavior agrees with the evolution law of K_L. For instance, at 100 K we obtained an isotropic K_L of 0.5 $Wm^{-1}K^{-1}$ in both directions. This value decreased to 0.2 $Wm^{-1}K^{-1}$ at 300 K. The low K_L at 300 K may be an indication of relatively stronger phonon-phonon interaction leading to substantial anharmonic scattering. Due to this stronger scattering, the phonon mean free path will be decreased, and this may result in low K_L. Overall, we found that the total thermal conductivity of the system was mostly governed by the K_e. For comparison, we present the total thermal conductivity of the V_2S_2O monolayer with other well-studied MoS_2 in Supplementary Table 1.Finally, we evaluated the spin and charge dimensionless figure of merit (*ZT*). We obtained the dimensionless *ZT* using the transport parameters in the relations:

$$ZT_{spin} = \frac{\sigma S_{eff-spin}{}^2 T}{K_e + K_L} \quad (14)$$

$$ZT_{Charge} = \frac{\sigma S_{eff-Charge}{}^2 T}{K_e + K_L} \quad (15)$$

where $\sigma = \sigma^{\uparrow} + \sigma^{\downarrow}$, and K_e is the sum of the electronic part of the thermal conductivities of the spin-down and spin-up carriers. Figure 6A-D reveals the computed results. Due to the directional spin-dependence of the σ, we also obtained $ZT_{Charge} = ZT_{spin}$ along the y and x directions. At 300 K, we obtained a maximum *ZT* of 0.86 in the hole-doped systems, while it became 0.63 in the electron-doped systems.

This carrier type dependent *ZT* feature comes from the electrical conductivity in which $\sigma^{\uparrow}(\sigma^{\downarrow})$ is greater in the hole-doped system along the y-direction (x-direction). Overall, the *ZT* is controlled by only one spin component in each direction. Our findings may suggest that the V_2S_2O altermagnet system may be used for potential pure spin current generation in spintronic and thermoelectricity.

CONCLUSIONS

We probed the spin-dependent transport properties of the altermagnet V_2S_2O monolayer using the spin-polarized density functional theory and Boltzmann transport theory. This V_2S_2O monolayer had a direct band gap of 1.15 eV and a uniform spin splitting of 0.51 eV at the X and Y points in the valence band maximum. This band gap was determined by the spin-down (spin-up) channels at the X-point (Y-point). We obtained a high critical temperature of about 746 K. Due to the directional spin-dependent feature in the band structure, the Seebeck coefficients, electrical conductivity, effective spin and charge Seebeck coefficients, electronic part of the thermal conductivity, and *ZT* are influenced by spin-down (spin-up) carriers in the x-direction (y-direction). The electrical conductivity obtained in the hole-doped systems is

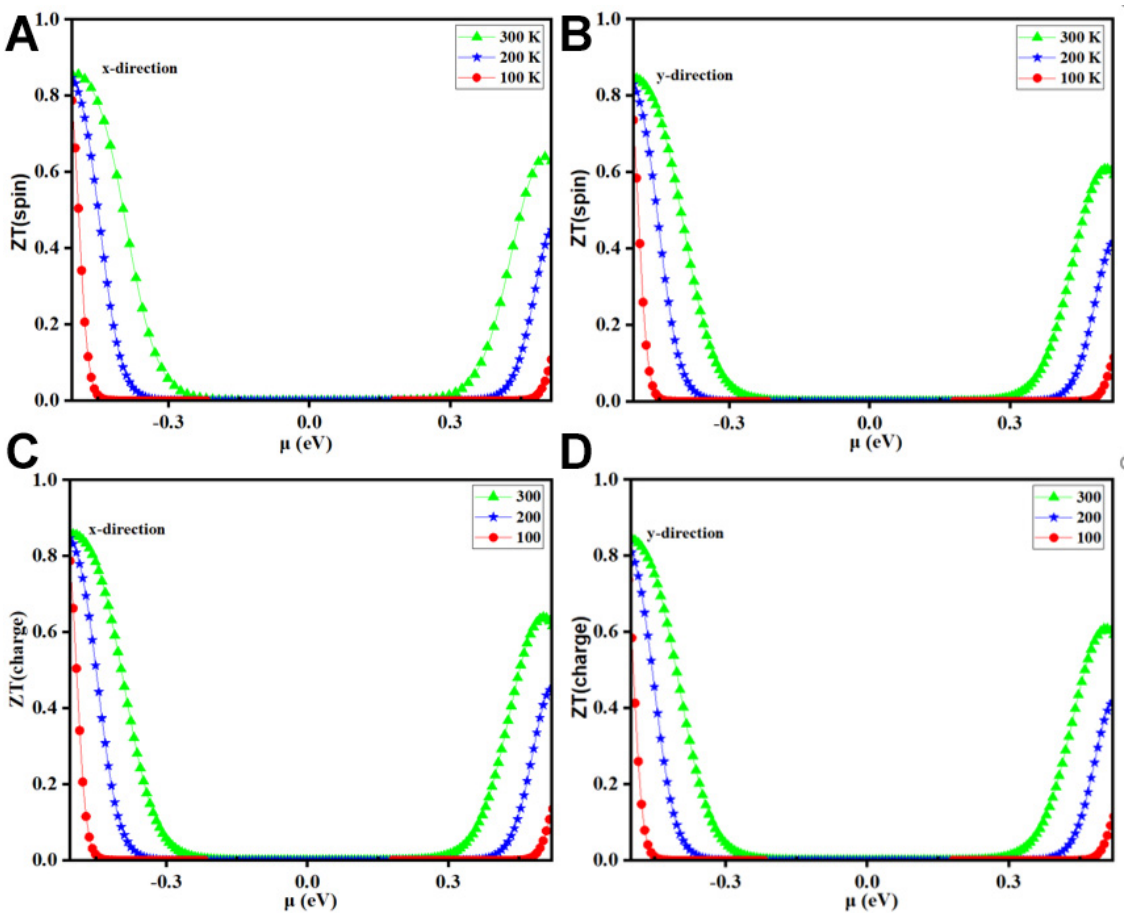

Figure 6. The dimensionless effective spin figure of merit in (A) x and (B) y-directions and the dimensionless charge figure of merit in (C) x and (D) y-directions *vs.* chemical potentials.

more than twice its value in the electron-doped systems in each direction at 300 K. We also found that the maximum magnitude of the effective spin and charge Seebeck coefficients was almost the same at all temperatures due to the orientational spin-dependent nature of the electrical conductivity. In the hole-doped systems, the electronic part of the thermal conductivities had higher values than in the electron-doped systems. We obtained a low isotropic K_L of about 0.2 $Wm^{-1}K^{-1}$ at 300 K. Essentially, the altermagnet V_2S_2O monolayer displayed a giant spin-dependent effective Seebeck coefficient of about 1.8 mVK^{-1} at 300 K and at a small electron or hole doping. This value is multiple times greater than reported values for most bulk and 2D materials. Besides, we also obtained $ZT_{Charge} = ZT_{spin}$. The maximum ZT was 0.86 for the hole-doped systems and 0.63 for the electron-doped systems. Overall, we suggest that V_2S_2O altermagnet may be used for potential pure spin-polarized current generation in spintronics and thermoelectric device applications.

DECLARATIONS

Authors' contributions

Conception of the idea and design of the study, data curation, formal analysis, writing an original draft, and revising the manuscript: Hong, J.

Performed DFT calculations and data curation, analyzed and interpreted the results, and wrote and revised the manuscript: Ashani, T.M.; Abdullah.

Availability of data and materials

The data that support the findings of this study are available from the corresponding author upon reasonable request.

Financial support and sponsorship

This work was supported by the National Research Foundation of Korea (NRF) grant funded by the Korean government (MSIT) (2022R1A2C1004440) and by the National Research Foundation of Korea (2022M3H4A1A040853)

Conflicts of interest

All authors declared that there are no conflicts of interest

Ethical approval and consent to participate

Not applicable.

Consent for publication

Not applicable.

REFERENCES

1. I; The PRX Editors. Editorial: altermagnetism-a new punch line of fundamental magnetism. *Phys. Rev. X.* **2022**, *12*, 04002. DOI
2. Manchon, A.; Koo, H. C.; Nitta, J.; Frolov, S. M.; Duine, R. A. New perspectives for Rashba spin-orbit coupling. *Nat. Mater.* **2015**, *14*, 871-82. DOI PubMed
3. Zhang, F.; Lv, L.; Xu, Z.; et al. Prediction of the TiS_2 bilayer with self-intercalation: robust ferromagnetic semiconductor with a high curie temperature. *J. Phys. Chem. C.* **2025**, *129*, 5577-88. DOI
4. Guo, S. D.; Tao, Y. L.; Wang, G.; Ang, Y. S. How to produce spin-splitting in antiferromagnetic materials. *J. Phys. Condens. Matter.* **2024**, *36*, 215804. DOI PubMed
5. Qi, Y.; Zhao, J.; Zeng, H. Spin-layer coupling in two-dimensional altermagnetic bilayers with tunable spin and valley splitting properties. *Phys. Rev. B.* **2024**, *110*, 014442. DOI
6. Ma, H. Y.; Hu, M.; Li, N.; et al. Multifunctional antiferromagnetic materials with giant piezomagnetism and noncollinear spin current. *Nat. Commun.* **2021**, *12*, 2846. DOI PubMed PMC
7. Guo, Y.; Liu, H.; Janson, O.; Fulga, I. C.; van, B. J.; Facio, J. I. Spin-split collinear antiferromagnets: a large-scale ab-initio study. *Materials. Today. Physics.* **2023**, *32*, 100991. DOI
8. Šmejkal, L.; Sinova, J.; Jungwirth, T. Beyond conventional ferromagnetism and antiferromagnetism: a phase with nonrelativistic spin and crystal rotation symmetry. *Phys. Rev. X.* **2022**, *12*, 031042. DOI
9. Šmejkal, L.; Sinova, J.; Jungwirth, T. Emerging research landscape of altermagnetism. *Phys. Rev. X.* **2022**, *12*, 040501. DOI
10. Naka, M.; Hayami, S.; Kusunose, H.; Yanagi, Y.; Motome, Y.; Seo, H. Spin current generation in organic antiferromagnets. *Nat. Commun.* **2019**, *10*, 4305. DOI PubMed PMC
11. Zhu, Y.; Chen, T.; Li, Y.; et al. Multipiezo effect in altermagnetic V_2SeTeO monolayer. *Nano. Lett.* **2024**, *24*, 472-8. DOI
12. Bhowal, S.; Spaldin, N. A. Ferroically ordered magnetic octupoles in d-wave altermagnets. *Phys. Rev. X.* **2024**, *14*, 011019. DOI
13. Guo, S.; Guo, X.; Cheng, K.; Wang, K.; Ang, Y. S. Piezoelectric altermagnetism and spin-valley polarization in Janus monolayer Cr_2 SO. *Appl. Phys. Lett.* **2023**, *123*, 082401. DOI
14. Gao, Z. F.; Qu, S.; Zeng, B.; et al. AI-accelerated discovery of altermagnetic materials. *arXiv* **2023**, arXiv:2311.04418. Available online: http://arxiv.org/abs/2311.04418 (accessed 2025-05-14).
15. Mazin, I. I. Altermagnetism in MnTe: origin, predicted manifestations, and routes to detwinning. *Phys. Rev. B.* **2023**, *107*, L100418. DOI
16. Mazin, I. I.; Koepernik, K.; Johannes, M. D.; González-Hernández, R.; Šmejkal, L. Prediction of unconventional magnetism in doped $FeSb_2$. *Proc. Natl. Acad. Sci. U. S. A.* **2021**, *118*, e2108924118. DOI PubMed PMC
17. Sødequist, J.; Olsen, T. Two-dimensional altermagnets from high throughput computational screening: symmetry requirements, chiral magnons, and spin-orbit effects. *Appl. Phys. Lett.* **2024**, *124*, 182409. DOI
18. Zeng, S.; Zhao, Y. Description of two-dimensional altermagnetism: categorization using spin group theory. *Phys. Rev. B.* **2024**, *110*, . 054406. DOI

19. Occhialini, C. A.; Martins, L. G. P.; Fan, S.; et al. Strain-modulated anisotropic electronic structure in superconducting RuO_2 films. *Phys. Rev. Materials.* **2022**, *6*, 084802. DOI
20. Gonzalez, B. R. D.; Zubáč, J.; Gonzalez-Hernandez, R.; et al. Spontaneous anomalous hall effect arising from an unconventional compensated magnetic phase in a semiconductor. *Phys. Rev. Lett.* **2023**, *130*, 036702. DOI
21. Šmejkal, L.; Hellenes, A. B.; González-hernández, R.; Sinova, J.; Jungwirth, T. Giant and tunneling magnetoresistance in unconventional collinear antiferromagnets with nonrelativistic spin-momentum coupling. *Phys. Rev. X.* **2022**, *12*, 011028. DOI
22. Ahn, K.; Hariki, A.; Lee, K.; Kuneš, J. Antiferromagnetism in RuO_2 as *d*-wave pomeranchuk instability. *Phys. Rev. B.* **2019**, *99*, 184432. DOI
23. Hayami, S.; Yanagi, Y.; Kusunose, H. Momentum-dependent spin splitting by collinear antiferromagnetic ordering. *J. Phys. Soc. Jpn.* **2019**, *88*, 123702. DOI
24. Yuan, L.; Wang, Z.; Luo, J.; Rashba, E. I.; Zunger, A. Giant momentum-dependent spin splitting in centrosymmetric low-Z antiferromagnets. *Phys. Rev. B.* **2020**, *102*, 014422. DOI
25. Sukhachov, P. O.; Hodt, E. W.; Linder, J. Thermoelectric effect in altermagnet-superconductor junctions. *Phys. Rev. B.* **2024**, *110*, 094508. DOI
26. Bai, H.; Zhang, Y. C.; Zhou, Y. J.; et al. Efficient spin-to-charge conversion via altermagnetic spin splitting effect in antiferromagnet RuO_2. *Phys. Rev. Lett.* **2023**, *130*, 216701. DOI
27. Lyu, K.; Li, Y. Orientation-dependent spin-polarization and transport properties in altermagnet based resonant tunneling junctions. *Results. Phys.* **2024**, *59*, 107564. DOI
28. Fedchenko, O.; Minár, J.; Akashdeep, A.; et al. Observation of time-reversal symmetry breaking in the band structure of altermagnetic RuO_2. *Sci. Adv.* **2024**, *10*, eadj4883. DOI
29. Krempaský, J.; Šmejkal, L.; D'Souza, S. W.; et al. Altermagnetic lifting of Kramers spin degeneracy. *Nature* **2024**, *626*, 517-22. DOI PubMed PMC
30. Fan, Y.; Wang, Q.; Wang, W.; et al. Robust magnetic-field-free perpendicular magnetization switching by manipulating spin polarization direction in RuO_2/[Pt/Co/Pt] heterojunctions. *ACS. Nano.* **2024**, *18*, 26350-8. DOI
31. Kresse, G.; Furthmüller, J. Efficiency of ab-initio total energy calculations for metals and semiconductors using a plane-wave basis set. *Comput. Mater. Sci.* **1996**, *6*, 15-50. DOI
32. Kresse, G.; Furthmüller, J. Efficient iterative schemes for ab initio total-energy calculations using a plane-wave basis set. *Phys. Rev. B.* **1996**, *54*, 11169. DOI
33. Perdew, J. P.; Burke, K.; Ernzerhof, M. Generalized gradient approximation made simple. *Phys. Rev. Lett.* **1996**, *77*, 3865-8. DOI PubMed
34. Dion, M.; Rydberg, H.; Schröder, E.; Langreth, D. C.; Lundqvist, B. I. Van der Waals density functional for general geometries. *Phys. Rev. Lett.* **2004**, *92*, 246401. DOI
35. Pack, J. D.; Monkhorst, H. J. "Special points for Brillouin-zone integrations"-a reply. *Phys. Rev. B.* **1977**, *16*, 1748. DOI
36. Heyd, J.; Scuseria, G. E.; Ernzerhof, M. Hybrid functionals based on a screened Coulomb potential. *J. Chem. Phys.* **2003**, *118*, 8207-15. DOI
37. Heyd, J.; Scuseria, G. E.; Ernzerhof, M. Erratum: "Hybrid functionals based on a screened Coulomb potential" [J. *J. Chem. Phys.* **2006**, *124*, 219906. DOI
38. Vampire Curie temperature simulation tutorial. https://vampire.york.ac.uk/tutorials/simulation/curie-temperature/ (accessed 2025-05-14).
39. Madsen, G. K.; Singh, D. J. BoltzTraP. A code for calculating band-structure dependent quantities. *Comput. Phys. Commun.* **2006**, *175*, 67-71. DOI
40. Togo, A.; Chaput, L.; Tanaka, I. Distributions of phonon lifetimes in Brillouin zones. *Phys. Rev. B.* **2015**, *91*, 094306. DOI
41. Yu, Y. High storage capacity and small volume change of potassium-intercalation into novel vanadium oxychalcogenide monolayers V_2S_2O, V_2Se_2O and V_2Te_2O: an ab initio DFT investigation. *Appl. Surf. Sci.* **2021**, *546*, 149062. DOI
42. Evans, R. F.; Fan, W. J.; Chureemart, P.; Ostler, T. A.; Ellis, M. O.; Chantrell, R. W. Atomistic spin model simulations of magnetic nanomaterials. *J. Phys. Condens. Matter.* **2014**, *26*, 103202. DOI PubMed
43. Casu, G.; Bosin, A.; Fiorentini, V. Efficient thermoelectricity in $Sr_2Nb_2O_7$ with energy-dependent relaxation times. *Phys. Rev. Materials.* **2020**, *4*, 075404. DOI
44. Marfoua, B.; Hong, J. Graphene induced high thermoelectric performance in ZnO/graphene heterostructure. *Adv. Mater. Interfaces.* **2023**, *10*, 2202387. DOI
45. Ullah, A.; Bezzerga, D.; Hong, J. Giant spin seebeck effect with highly polarized spin current generation and piezoelectricity in flexible V_2SeTeO altermagnet at room temperature. *Mater. Today. Phys.* **2024**, *47*, 101539. DOI
46. Jaworski, C. M.; Yang, J.; Mack, S.; Awschalom, D. D.; Heremans, J. P.; Myers, R. C. Observation of the spin-Seebeck effect in a ferromagnetic semiconductor. *Nat. Mater.* **2010**, *9*, 898-903. DOI
47. Reitz, D.; Li, J.; Yuan, W.; Shi, J.; Tserkovnyak, Y. Spin Seebeck effect near the antiferromagnetic spin-flop transition. *Phys. Rev. B.* **2020**, *102*, 020408. DOI
48. Wadhwa, P.; Bosin, A.; Filippetti, A. Giant spin-dependent Seebeck effect from fully spin-polarized carriers in n-doped $EuTiO_3$: a prototype material for spin-caloritronic applications. *J. Mater. Chem. A.* **2023**, *11*, 6842-53. DOI
49. Priyanka D, Venkatesh G, Srinivasan M, Palanisamy G, Ramasamy P. Half metallic heusler alloys XMnGe (X = Ti, Zr, Hf) for spin

flip and thermoelectric device application - material computations. *Mater. Sci. Semicond. Process.* **2023**, *159*, 107367. DOI